PAPER

The role of copper in the synthesis of platinum based catalysts and in their efficiency for the hydrogen evolution reaction†

Geanina Mihai, [ID] [a] Liana Anicai,[a] Laura-Bianca Enache,[a] Oana Lazar, [ID] [a] Marius Enachescu, [ID] [a] Bostjan Genorio [ID] [b] and Ayrat M. Dimiev [ID] *[ac]

In this work, we synthesized two hybrid copper–platinum composites and two mono-metallic control samples on the carbon black (CB) support with the use of the polyol-formaldehyde method. The bi-metallic composites were prepared by the two different experimental protocols: consecutive deposition of the two metals CB/CuPt-1 and co-deposition of CB/CuPt-2. With both methods, the use of copper facilitates deposition of platinum, leading to a higher platinum content in the products, compared to the mono-metallic CB/Pt control sample. SEM and HRTEM images show that, in monometallic CB/Cu, copper does not form any nanoparticles, being atomically dispersed on the CB surface. The other three samples have uniformly dispersed nanoparticles with a size of 2–4 nm, densely covering the CB support. XRD and XPS data suggest that copper facilitates more efficient reduction of platinum, and is incorporated into the nanoparticles. Next, all the synthesized composites were tested for the hydrogen evolution reaction (HER). The two bi-metallic composites outperform not only the mono-metallic CB/Pt sample, but also the commercial catalyst with a similar or an even higher platinum content. Interestingly, the catalytic efficiency is not directly related to the platinum content in the tested materials. As a result, CB/CuPt-2, which has a lower Pt content, demonstrates greater efficiency in certain parameters compared to CB/PtCu-1, which contains a higher Pt content. This observation suggests that incorporation of copper into the structure of the composite materials leads to synergistic effects. Our results show the role of copper in the efficiency of the platinum catalysts for the HER and open routes for increasing the efficiency of the hydrogen generation reaction on an industrial scale.

1. Introduction

The habitual use of traditional sources of energy for many decades has led to an environmental and energy crisis, which could be resolved by development of alternative energetics, in particular the hydrogen based energetics.[1–4] However, its successful implementation is hampered by the lack of efficient and environmentally friendly hydrogen generation technology. The current electrochemical water splitting technique is based on the use of expensive noble metal catalysts, mostly platinum.[5–9] The ever increasing demand and limited resources of platinum stimulate the search for alternative cost-efficient and readily available catalysts, the electrocatalytic activity of which will be comparable to the commercial products. Another problem is the efficiency and stability of the catalysts.

Nowadays, numerous studies are devoted to solving these tasks. One of the common approaches is designing bimetallic catalysts, in which noble metals (Pt and Pd) are partially replaced by less expensive 3d-metals (Co, Ni, and Cu).[10–13] In this direction, the most straightforward element for alloying Pt is Cu, due to the close matching lattice parameters of the two metals.[14,15] The overall alloying effect is explained by introducing the lattice strain, thus enhancing the electrocatalytic activity of Pt alloy catalysts.[16,17] In particular, the (111) plane of PtCu was found to be especially active for the hydrogen evolution reaction (HER).[18]

Concerning the alloying ratio, the catalyst with a Pt/Cu ratio of 3/1 was reported as the most active one among other tested ratios, and outperformed the commercial catalysts.[19] In another study, the Pt/Cu ratio of 1/3 was found to be the most efficient.[20]

In recent years, various investigations have been performed dealing with the synthesis and application of PtCu nanostructures

[a] *Center of Surface Science and Nanotechnology, National University of Science and Technology Politehnica Bucharest, Splaiul Independentei 313, Bucharest, 060042, Romania. E-mail: dimiev.labs@gmail.com*

[b] *Faculty of Chemistry and Chemical Technology, University of Ljubljana, Ljubljana, Slovenia*

[c] *Department of Chemistry, Rice University, Houston, TX, 77005, USA*

† Electronic supplementary information (ESI) available. See DOI: https://doi.org/10.1039/d5nj00667h

Table 1 PtCu-based electrocatalysts and their HER performance

Catalyst	Electrode/substrate	Electrolyte	Tafel slope (mV dec^{-1})	Stability	Ref.
Pt_2Cu_1/CB	Carbon paper	0.5 M H_2SO_4	56.87	—	20
Pt_1Cu_1/CB	Carbon paper	0.5 M H_2SO_4	54.16	—	20
Pt_1Cu_3/CB	Carbon paper	0.5 M H_2SO_4	29.72	1000 CV cycles	20
Pt_2Cu_1/CB	Carbon paper	1 M KOH	93.37	—	20
Pt_1Cu_1/CB	Carbon paper	1 M KOH	97.86	—	20
Pt_1Cu_3/CB	Carbon paper	1 M KOH	128.46	1000 CV cycles	20
PtCu nanospheres/C	Glassy carbon	0.5 M H_2SO_4	28.4	5000 CV cycles	21
PtCu hierarchical branched nanodendrites (HBNDs)	Glassy carbon	0.5 M H_2SO_4	30	5000 CV cycles	22
Pt_1Cu_1 nanotubes (NTs)	Carbon paper	0.5 M H_2SO_4	51	10 000 CV cycles	23
Pt_1Cu_2 nanotubes (NTs)	Carbon paper	0.5 M H_2SO_4	80	10 000 CV cycles	23
Pt_5Cu_2 nanotubes (NTs)	Carbon paper	0.5 M H_2SO_4	27	10 000 CV cycles	23
PtCu nanospheres	WO_3 deposited on Cu foam (CF) carbon cloth	0.5 M H_2SO_4	40–60 Depending on the activation procedure	2000 CV cycles	24
PtCu-Mo2C@C	Glassy carbon	0.5 M H_2SO_4	36	5000 CV cycles	25
PtCu dodecahedral nanoframes (DNFs)/CB	Glassy carbon	0.5 M H_2SO_4	34	1000 CV cycles	18
PtCu dodecahedral nanoframes (DNFs)/CB	Glassy carbon	0.5 M KOH	55	1000 CV cycles	18
PtCu	Cu foam (CF)	0.5 M H_2SO_4	42.29	100 h	26
$Pt_{0.55}Cu_{0.45}$ nanoparticles	Carbon rod	1 M KOH	148.4	500 CV cycles	19
$Pt_{0.75}Cu_{0.25}$ nanoparticles	Carbon rod	1 M KOH	35.5	500 CV cycles	19

in the field of the HER.[13,18–26] Li et al.[21] prepared 3D PtCu nanospheres (NSs) consisting of nano-single crystal particles by applying a simple aqueous solution method. They were characterized by a Pt-rich surface structure and exhibited superior HER electrocatalytic activity and durability in acidic media compared to the commercial Pt/C catalyst. Du et al.[22] fabricated PtCu hierarchical branched nanodendrites (HBNDs) with tunable branches, size, and composition using an air oxidative induced dealloy process. The obtained PtCu HBNDs showed enhanced HER activity and superior durability due to the larger open porous structure, more accessible active sites and electronic synergistic effects between Pt and Cu atoms. Zhang et al.[18] reported the synthesis of PtCu dodecahedral nanoframes (PtCu DNFs) characterized by a large specific surface area and abundant active sites, which exhibited excellent HER catalytic performance in both acidic and alkaline electrolytes. Some of the recently developed PtCu-based electrocatalysts as well as their HER performance are presented in Table 1.

Utilization of nanoscale metallic species as a catalyst requires a structural support. For electrocatalysts, such a support must be electrically conductive. From these perspectives, carbon black (CB) is a cheap, readily available material, actively used in commercial samples. From these perspectives, the results reported in the work[19] are expectable, since the PtCu nanoparticles were deposited straight on the glassy carbon electrode without any structural support; thus, the content of Pt was significantly higher than that in commercial catalysts. In another study, the CB/PtCu catalyst was prepared in a complex multi-step procedure: the PtCu nanoparticles were first synthesized separately and then deposited on CB which require the use of numerous solvents such as oleylamine, oleic acid, ethanol, hexane, butylamine, and methanol.[20]

Overall, these reported investigations suggest that PtCu-based nanostructures could act as attractive catalysts in electrochemical applications related to hydrogen production through water electrolysis. However, their efficiency is strongly dependent on their synthesis procedure, composition and morphology.[19] The relationship between the synthetic protocols, resulted structure, and catalytic efficiency is not yet clear. Moreover, many studies used multi-step complex synthetic protocols.

Thus, new simple and eco-friendly synthetic procedures are desired to synthesize the CB/PtCu catalysts. In this work, we synthesized the two CB/PtCu catalysts by two alternative synthetic protocols, analyzed their structure, and tested their catalytic activity toward the acidic hydrogen evolution reaction.

2. Experimental part

2.1. Materials

In order to perform experiments, all chemical reagents used were of analytical grade and supplied by Sigma Aldrich and Alfa Aesar. They were used as received without any further purification.

2.2. The preparation of the catalyst samples

All the samples were prepared using the same procedure. The targeted metal content in all the samples was 10% with respect to metals, i.e. the CB/metal ratio was 9/1.

2.2.1. Preparation of CB/Pt. 180 mg of carbon black (CB) was dispersed in 15 g of isopropanol (IPA) by sonication with a tip sonicator for 10 min. Then, 22 g of ethylene glycol (EG) were added and sonicated for another 10 min. The dispersion was transferred to a round bottom flask and heated to 85 °C with constant stirring with a magnetic stirrer, which continued during the rest of the synthesis. In a separate flask, 50 mg of K_2PtCl_6 was dissolved in 4 g of distilled water at 80 °C. The hot K_2PtCl_6 solution was added to the CB dispersion dropwise within 1 min upon constant stirring with a magnetic stirrer. The temperature was increased to 91 °C and stirred for 40 min to allow most of the IPA to evaporate. Next, the flask was equipped with a reverse condenser; 0.9 g of the 35% formaldehyde solution was added dropwise within 1 min, and stirring of

the dispersion was continued for 15 min. Then, another 0.9 g of the formaldehyde solution was added, and the mixture was stirred for 2 h. After 2 h stirring, the flask was removed from the oil bath and allowed to cool naturally. After cooling, the mixture was diluted with 30 mL of distilled water and filtered through a polymer filter with suction. The filter cake was redispersed in 100 mL of distilled water, stirred for 5 min and filtered again. Such purification was repeated three more times, and the purified product was dried in open air. This yields the sample denoted as CB/Pt, which served as the 1st control sample, containing only Pt.

2.2.2. Preparation of CB/Cu. The second control sample, containing only the Cu metal, was prepared using the same procedure. The aqueous $CuSO_4$ solution with a concentration of 1% with respect to Cu was used as the copper source. This sample was denoted as CB/Cu.

The two bimetallic samples were prepared in two different ways.

2.2.3. Preparation of CB/CuPt-1. To prepare the first bimetallic sample, Cu and Pt were deposited on CB consecutively, one by one. First, the dispersion of CB in IPA was mixed with the aqueous 1% $CuSO_4$ solution in a CB/Cu ratio of 9/1 and stirred for 3 h. Then, the product was filtered, washed with water to remove excess non-anchored copper, and dried in open air. The as-obtained dry precursor material (CB–Cu-precursor) was then used as a substrate to deposit Pt as described above in Section 2.2.1. The used CB–Cu-precursor/Pt ratio was 9/1.

2.2.4. Preparation of CB/CuPt-2. To prepare the second bimetallic sample CB/CuPt-2, copper and platinum were co-deposited on CB simultaneously. During preparative steps, the warm $CuSO_4$ solution was mixed with the hot K_2PtCl_6 solution; no visual change was observed upon mixing the two solutions, and the summative solution remained transparent. This solution was then mixed with the CB dispersion in IPA as described in Section 2.2.1. The targeted mixing ratio was CB/Cu/Pt = 9/1/1.

2.3. Characterization

XRD analysis was conducted with a Rigaku High Resolution SmartLab X-ray diffractometer, 9 kW, with a rotating anode, using $Cu_{K\alpha}$ radiation (λ = 0.15406 nm) at room temperature, in the 2θ range of 5–120 degrees.

The morphology and composition of the samples were analyzed using a Hitachi SU8230 scanning electron microscope (SEM) coupled with an Oxford Instruments energy dispersive X-ray spectroscope (EDX). Secondary electron images were acquired at different magnifications using an accelerating voltage of 10 kV for all samples.

The morphological properties of the synthesized samples were also investigated through the high resolution-scanning transmission electron microscopy technique using a Hitachi HD-2700 instrument operating at a 200 kV accelerating voltage, equipped with an energy dispersive X-ray (EDX) Oxford Instruments X-max 100 TLE detector. Three types of electron images were acquired simultaneously, at the same magnification and in the same location on the sample, by using three different imaging techniques: secondary electrons (SE), the high angle

annular dark field technique for ZC–phase contrast imaging and the bright field technique for transmission electron (TE) imaging.

X-ray photoelectron spectroscopy (XPS) measurements were conducted using a Versa Probe 3 AD (PHI, Chanhassen, USA) instrument, equipped with a monochromatic Al Kα X-ray source. The source operated at an accelerating voltage of 15 kV and an emission current of 13.3 mA. Powder samples were mounted on double-sided Scotch tape and positioned at the center of the XPS holder. Spectra were acquired for each sample over a 1 × 1 mm analysis area, with the charge neutralizer activated during data collection. Survey spectra were recorded using a pass energy of 224 eV and a step size of 0.8 eV. High-resolution (HR) spectra were recorded with a pass energy of 27 eV and a step size of 0.1 eV. To ensure high-quality spectral data with a good signal-to-noise ratio, at least 10 sweeps were performed for each measurement. The energy scale of the XPS spectra and any possible charging effects were corrected by referencing the C=C peak in the C 1s spectrum of the carbon support, with a binding energy (BE) of 284.5 eV. Spectral deconvolution was carried out using MultiPak 9.9.1 software, and Shirley background correction was applied to all spectra.

2.4. Electrochemical investigations

To assess the electrocatalytic activity of the synthesized nanostructured composite powders for the hydrogen evolution reaction (HER), a classical three-electrode configuration cell was used. A glassy carbon electrode coated with the investigated nanostructured powders acted as the working electrode (with a constant geometrical surface of 0.196 cm^2), while a large area Pt plate and an Ag/AgCl electrode were employed as an auxiliary electrode and a reference electrode, respectively. The cell was connected to a PARSTAT 4000 potentiostat controlled with VersaStudio software. The cathodic linear polarization curves were recorded in 0.5 M H_2SO_4 aqueous solution at a scan rate of 10 mV s^{-1} at 25 °C. Tafel slopes were determined from HER polarization curves.

In order to determine the electrochemical active surface area (ECSA), cyclic voltammograms (CVs) were recorded in 0.1 M $HClO_4$ aqueous solution at a scan rate of 50 mV s^{-1} at 25 °C. An initial pre-treatment consisting of 50 cycles at 100 mV s^{-1} in 0.1 M $HClO_4$ was performed to obtain a clean and reproducible surface. Then, 2 cycles were recorded in the same range of potentials but at 50 mV s^{-1} and the 2nd CV was used to calculate the ECSA. To estimate the ECSA (m^2 g^{-1}), the hydrogen adsorption/desorption area was taken into consideration, using eqn (1) shown below:[27,28]

$$\text{ECSA} = \frac{Q_H}{m \times 0.21} \times 10^{-4} \qquad (1)$$

where Q_H represents the coulombic charge for hydrogen desorption (mC), m is the mass of the powder on the electrode (g) and 0.21 is the charge required to oxidize a monolayer of H_2 on cleaned Pt (mC cm^{-2}).

Typically, about 5 mg of CB/Cu, CB/Pt, CB/PtCu (both synthesis routes) and C-Pt 10 commercial powders were

dispersed, and 2 mL of water, 250 μL of isopropilic alcohol and 26 μL of Nafion were added. Then, the dispersion was subjected to ultrasound stirring for 45 min at room temperature. An aliquot of 10 μL of the homogenized suspension was applied onto the GC surface, followed by drying in an oven at 40 °C for 4 h. The final electrocatalyst amount was 112 μg cm^{-2}.

In another sequence of experiments, to assess the durability of the synthesized CB/PtCu nanostructured powders, 500 CV cycles were applied at a scan rate of 100 mV s^{-1} in 0.5 M H$_2$SO$_4$ solution.

Additionally, the hydrogen amount produced during electrolysis of aqueous 0.5 M H$_2$SO$_4$ was measured involving Hofmann's cell, equipped with the investigated composites as the working electrode and a Pt plate as the counter electrode. Under this sequence of experiments, 60 μL of each catalyst ink was drop-casted onto electrochemically grown Ni nanofoams used as metallic substrates (having a constant geometrical surface of 2 cm^2) and the as-prepared cathodic electrodes were then air-dried at 40 °C for 4 h. The cathodic efficiency of the HER (η) was then determined for various applied current densities. The yield of hydrogen gas was calculated by making use of the current I (A) passing from the cell for a measured period of time t (s) and the volume I (cm^3) of H, using the formula shown below[29]:

$$\eta = \frac{2F(V/V_m)}{I \times t} = \frac{7.89V}{I \times t} \tag{2}$$

where F is the Faraday constant, F = 96 500 C mol^{-1}; V_m is the molar volume of hydrogen at 25 °C, in cm^3; I is the total applied current, in A; t is the electrolysis duration, in s; V is the volume of gas, in cm^3.

3. Results and discussion

Fig. 1 presents the XRD pattern of the four synthesized samples. The XRD pattern of CB exhibits two major peaks at 25.5° 2θ and 44.49° 2θ. These signals are consistent with C(0,0,2) and C(1,1,1) reflections for CB. Another weak signal at 82.0° 2θ most likely corresponds to the C(1,1,2) plane of CB.[30] CB/Cu does not contain any additional reflections on top of those for CB, suggesting that copper does not form crystalline structures on the CB substrate. The second control sample CB/Pt exhibits additional peaks at 39.8°, 46.2°, and 67.9° 2θ, which are consistent, respectively, with the (1,1,1), (2,0,0), and (2,2,0) planes of metallic Pt. The same three additional reflections are present in the XRD patterns of the two bimetallic products CB/CuPt-1 and CB/CuPt-2. Notably, position of the (1,1,1) signal shifts from 39.8° for CB/Pt to 40.1° for CB/CuPt-1 and to 40.3° for CB/CuPt-2. This decrease of the lattice parameters serves as indirect evidence for incorporating Cu atoms with a smaller ionic radius. Also, the signal-to-noise ratio for CB/CuPt-2 is lower than those for CB/Pt and CB/CuPt-1, suggesting lower crystallinity of the formed nanoparticles.
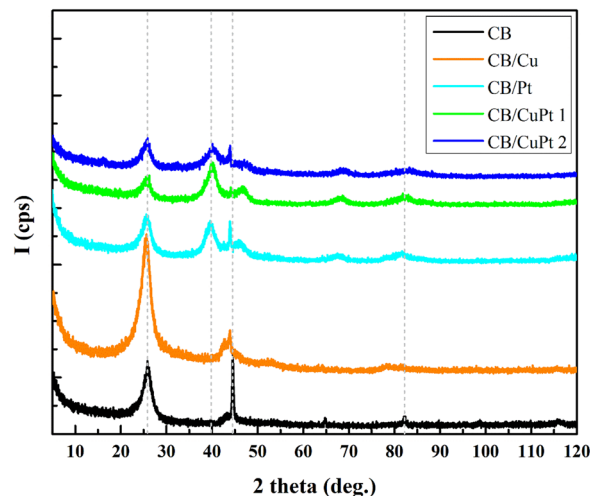

Fig. 1 XRD diffractograms of the four samples and the CB support.

Based on Scherrer's equation, the mean crystallite sizes were computed as follows:

$$D_{hkl} = \frac{k \times \lambda}{\beta_{hkl} \times \cos(\theta)} \tag{3}$$

where D_{hkl} is the crystallite size in the direction perpendicular to the lattice planes (hkl); k is Scherrer's constant; λ (0.15406 nm) is the X-ray wavelength in nm; β_{hkl} is the peak width at half-maximum peak height and θ is the half angle of the diffraction peak.[31]

The crystallite sizes (in nm) were calculated for the (1,1,1) reflection peak of Pt and the results obtained are presented in Table 2.

Fig. 2 presents SEM images of the four samples. Spherical particles of the CB support with a size of 50–80 nm are well

Table 2 Crystallite sizes determined based on Scherrer's equation

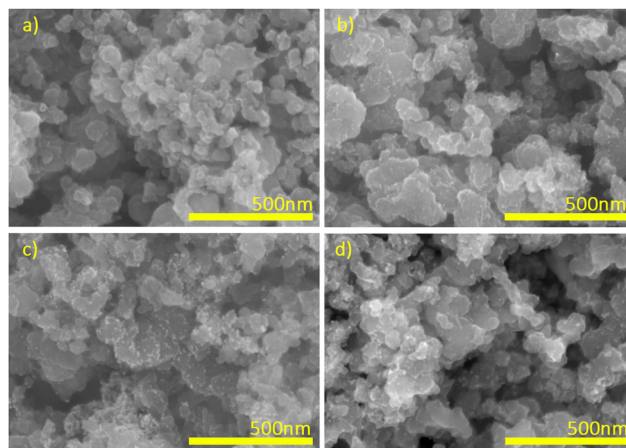| Reflection	CB/Pt	CB/CuPt 1	CB/CuPt 2
(1,1,1) Pt	3.07	3.74	3.73

Fig. 2 SEM images of the samples: CB/Cu (a), CB/Pt (b), CB/CuPt-1 (c), and CB/CuPt-2 (d).

Table 3 The elemental content in the four samples based on the EDX data

Elements	CB/Cu		CB/Pt		CB/CuPt-1		CB/CuPt-2	
	at%	wt%	at%	wt%	at%	wt%	at%	wt%
Cu	0.5	2.8			0.3	1.4	0.7	3.1
Pt			0.6	8.3	0.9	10.8	0.7	9.2

Table 4 The elemental content in the four samples based on the XPS data

Content (at%)	CB/Cu	CB/Pt	CB/CuPt-1	CB/CuPt-2
Cu	0.4		0.6	0.7
Pt		1.0	1.5	1.2

visible in the images of all the four samples. In addition, the three samples, CB/Pt, CB/CuPt-1, and CB/CuPt-2, contain small brighter contrast dots, associated with the formed metal nanoparticles.

The elemental content for the four samples based on the EDX and XPS data is presented in Tables 3 and 4, respectively. There are some discrepancies between the data obtained by the two methods. However, the trend observed for the samples is the same based on both methods. The first observation is that only a small part of copper is deposited on CB using the polyol method: CB/Cu contains only 2.82 wt% copper instead of the targeted 10%. Next, co-deposition with platinum increases the copper content: 3.06 wt% in CB/CuPt-2 compared to the 2.82 wt% in CB/Cu. The same is observed for the deposition of platinum. Both CB/CuPt-1 and CB/CuPt-2 contain more platinum. For CB/CuPt-2, this observation can be explained by co-deposition of the metals. The surprising observation is the high platinum content in CB/CuPt-1, obtained using both methods. It demonstrates the highest platinum content among all the three platinum containing samples, especially when measured by XPS. This observation suggests that the low content of atomically dispersed copper on the CB surface facilitates deposition of platinum (Tables 3 and 4).

Note, in CB/CuPt-1 and in CB/CuPt-2, some copper may exist on the CB surface separately from platinum particles due to the used synthetic procedures. This is why the position of the (1,1,1) reflections is not consistent with the Pt/Cu ratio as one might expect from the Vegard's Law perspective.[32,33]

Fig. 3 shows the XPS Pt 4f spectra of the three platinum containing samples. The spectra of each sample can be deconvoluted for the three components Pt(+4), Pt(+2), and Pt(0). The three components for the $4f_{5/2}$ signal appear at 76.4 eV, 75.7 eV and 74.9 eV, respectively. The components for the $4f_{7/2}$ signal appear at 72.9 eV, 72.2 eV, and 71.5 eV, respectively. At the first glance, the spectra for the three samples look similar. However, deconvolution shows that CB/Pt has a smaller Pt(0) component (61.9%), compared to that for CB/CuPt-1 (75.7%) and CB/CuPt-2 (77.3%). This observation can be explained by reduction of platinum oxides by copper, and/or by formation of hybrid alloyed structures, where copper donates its electrons to platinum.

The Cu 2p XPS spectra of the samples CB/Cu, CB/CuPt-1, and CB/CuPt-2 are shown in Fig. S1 (ESI†). The three spectra have a low signal/noise ratio due the lower copper content; thus, accurate deconvolution is not possible. However, one can see that the three spectra are very similar, i.e. the state of copper in the three samples is about the same.

HRTEM images give more information on the size and shape of the metal nanoparticles (Fig. 4). Here, again, for CB/Cu, one cannot see any particles, visible even at the highest magnification 1000k. This observation is consistent with the XRD data that show only carbon related reflexes in the
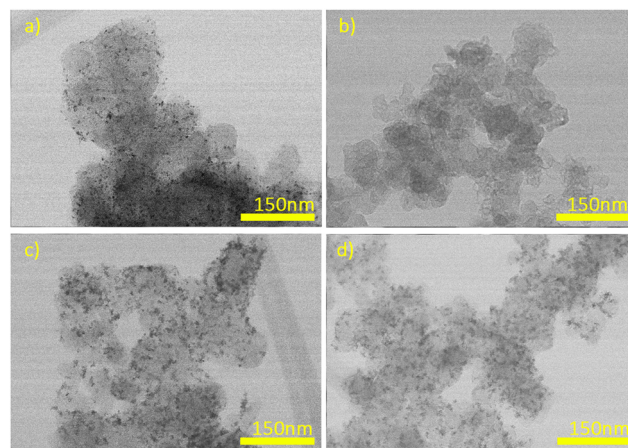
Fig. 4 HRTEM images of the samples: CB/Pt (a), CB/Cu (b), CB/CuPt-1 (c), and CB/CuPt-2 (d).
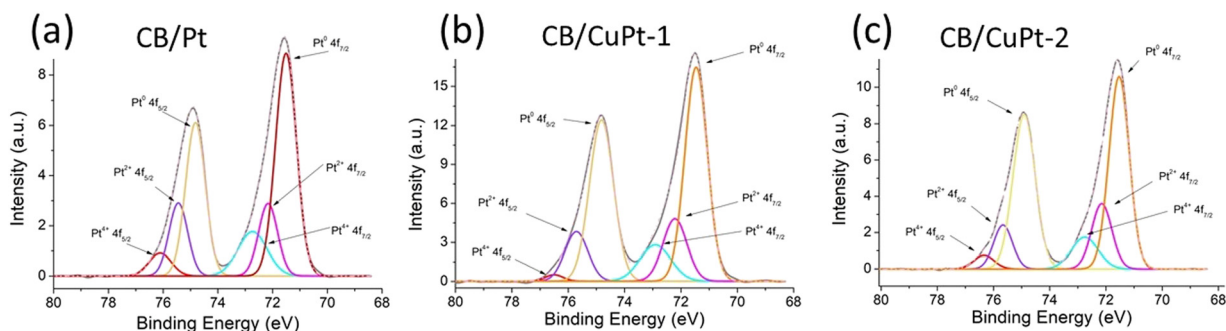
Fig. 3 XPS Pt 4f spectra of the three platinum containing samples: (a) CB/Pt, (b) CB/CuPt-1, and (c) CB/CuPt-2.
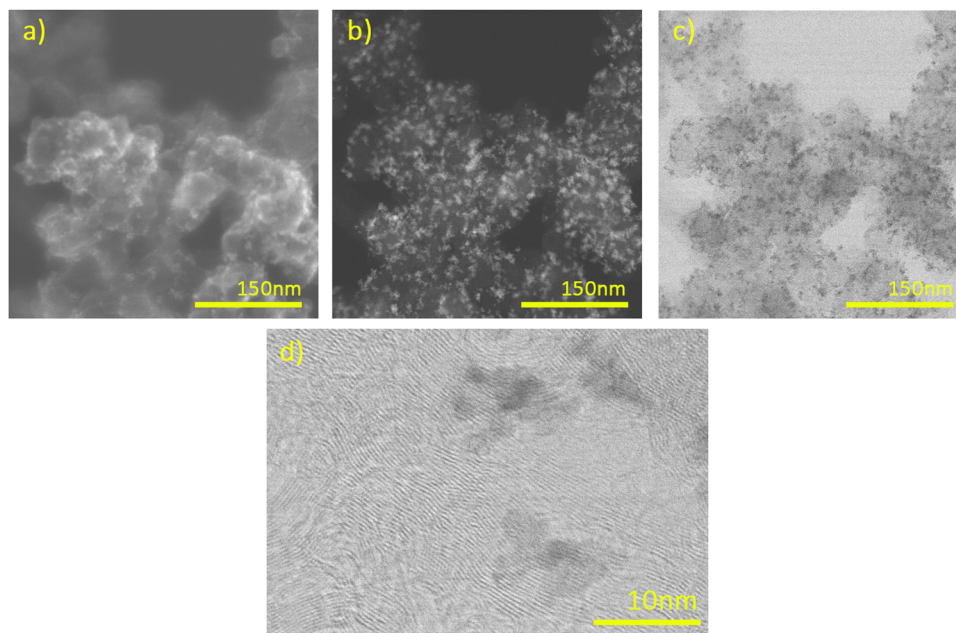
Fig. 5 Electron microscopy images of CB/CuPt-2, acquired in three different modes with the three different detectors: secondary electrons (a), phase contrast (b), and transmission electrons (c). (d) The ultra-high magnification UHRTEM image, acquired in the BF mode.

diffraction pattern (Fig. 1). Most likely, copper exists in the form of the single atoms or/and their clusters, invisible in the SEM images.

The other three samples have well-resolved particles with a size of 2–3 nm.

Fig. 5 presents three images for CB/CuPt-2, recorded at magnification 200k in the same location with three different detectors: SE – secondary electrons (a), ZC–phase contrast (b), and TE – transmission electrons (c). Similar images for other three samples are given in Fig. S2–S4 (ESI†). It should be noted that metal nanoparticles are not very visible in the SE mode. This is why they are barely distinguishable in the SEM images in Fig. 3. However, these particles are very well pronounced in the phase contrast and transmission modes.

Fig. 5d shows the ultra-high magnification bright field UHRTEM image of CB/CuPt-2. It clearly shows the layered structure of the CB particles, and the size of the CuPt particles with no visible lattice structure.

To summarize the characterization part, the platinum content in the three platinum containing samples slightly increases in the sequence CB/Pt < CB/CuPt-2 < CB/CuPt-1; the size of the particles is 2–4 nm in all three samples.

3.1. Electrocatalytic activity for the HER in 0.5 M H_2SO_4 electrolyte

The electrochemical activity of the synthesized composite nanopowders towards the HER was studied in 0.5 M H_2SO_4 electrolyte at room temperature and the corresponding recorded cathodic polarization curves are presented in Fig. 6a. The curve recorded for commercial C/Pt10 nanopowders was also included to compare the obtained results.

As shown in Fig. 6a, CB/Cu exhibits a very weak response against the HER, reaching a maximum current density of only 4.7 mA cm^{-2} at the most applied cathodic potential of −0.7 V *vs.* Ag/AgCl. This suggests that copper alone does not possess catalytic activity with respect to this reaction. This is why we exclude this sample from further considerations.

Enhanced electrocatalytic activity could be observed for both hybrid CB/CuPt composites as compared to commercial C/Pt10, able to achieve cathodic currents of 100 mA cm^{-2} for lower cathodic potentials, in the range −0.4 to −0.5 V *vs.* Ag/AgCl. The determined onset potentials (E_{onset}) for CB/Cu, commercial C/Pt10, CB/Pt, CB/CuPt-1 and CB/CuPt-2 exhibited values of −0.251 V, −0.232 V, −0.217 V, −0.211 V and −0.199 V, respectively. A displacement towards more positive values is evidenced in the case of CB/PtCu-1 and CB/PtCu-2, suggesting improved HER activity. Importantly, CB/CuPt-2 outperforms not only the commercial catalyst, but also CB/Pt prepared in this study using the same experimental protocol.

To gather more information on the electrocatalytic activity of the synthesized composites, Tafel analysis has been performed, considering the well-known kinetic equation:[34]

$$\eta = \frac{2.303RT}{\beta zF}\log i_0 - \frac{2.303RT}{\beta zF}\log i = a + b\log|i| \qquad (4)$$

where η represents the applied overpotential, i is the resulting (measured) current, b (V decade^{-1}) is the Tafel slope and a is the intercept related to the exchange current density i_0 the first term of eqn (4). Usually the Tafel slope (b) provides information on the HER mechanism and the exchange current density i_0 on the catalytic activity of the coating.[34,35]
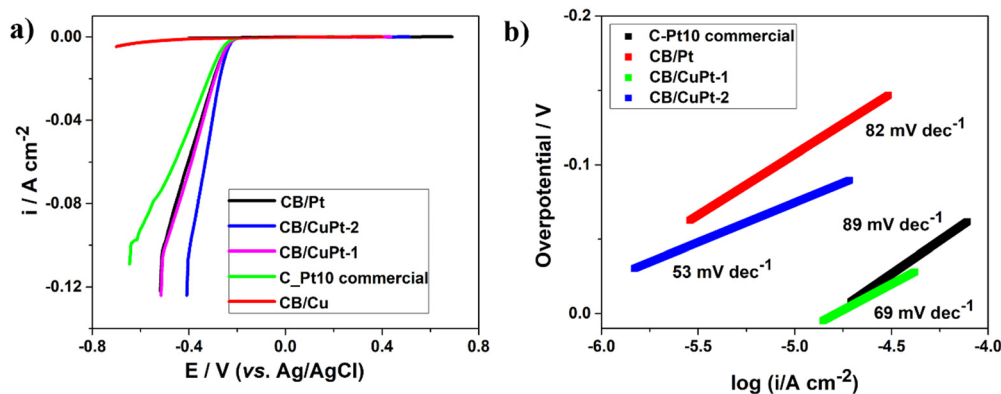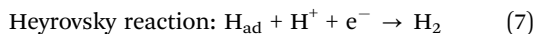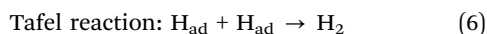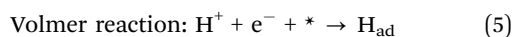
Fig. 6 (a) Polarization curves for the HER in 0.5 M H_2SO_4 for CB/Pt, CB/Cu, and CB/CuPt electrocatalysts. The scan rate is 10 mV s^{-1}. (For comparison the polarization curve for commercial C/Pt10 is also presented); (b) the corresponding Tafel plots.

As illustrated in Fig. 6(b), the Tafel slopes of CB/CuPt-1 (69 mV dec^{-1}) and CB/CuPt-2 (53 mV dec^{-1}) are smaller than those of CB/Pt (82 mV dec^{-1}) and commercial C/Pt10 (89 mV dec^{-1}), showing a faster reaction kinetics and more efficient HER.

According to the general models related to the HER mechanism in acidic media, a three-step reaction mechanism is considered to occur, respectively:

$$\text{Volmer reaction: } H^+ + e^- + * \rightarrow H_{ad} \qquad (5)$$

$$\text{Tafel reaction: } H_{ad} + H_{ad} \rightarrow H_2 \qquad (6)$$

$$\text{Heyrovsky reaction: } H_{ad} + H^+ + e^- \rightarrow H_2 \qquad (7)$$

If the Volmer reaction adsorption step is rate determining, the Tafel slope should be around 116 mV dec^{-1}, while if, the electrochemical desorption, the Heyrovsky step is rate determining, the Tafel slope would be about 40 mV dec^{-1}. For the Tafel desorption step as the rate-determining step, the Tafel slope should be about 30 mV dec^{-1}.[36,37]

It should be noted that the obtained Tafel slopes for CB/PtCu-1 and CB/PtCu-2 suggest that the Heyrovsky desorption step (eqn (7)) controls their HER kinetics. They are slightly higher than the theoretical value of 40 mV dec^{-1}, so that the presence of certain oxides that may impede the charge transfer is not excluded. In addition, the occurrence of the generated hydrogen micro-diffusion and interfacial diffusion through the microchannels in the catalyst layer to the surface of the catalyst layer could lower the overall H_2 mass transport process, as well.[37]

The more efficient HER in the presence of CB/CuPt-1 and CB/CuPt-2 as compared to CB/Pt and commercial C/Pt10 is apparently due to the synergistic effect between the two metals. Most likely, the incorporated Cu atoms alter the electronic structures of Pt, favorably influencing the affinity of the adsorbed H* species and further producing an improvement of the catalytic activity.[18,38] The difference in the Pt 4f XPS spectra supports this conclusion.

The determined values of exchange current densities and overpotentials at 1 and 10 mA cm^{-2} for the synthesized composites are presented in Table 5.

Table 5 Cathodic Tafel slopes, exchange current densities, and overpotentials at 1 and 10 mA cm^{-2} for the investigated catalysts

Sample	b/mV dec^{-1}	i_0/A cm^{-2}	η/mV ($i = 1$ mA cm^{-2})	η/mV ($i = 10$ mA cm^{-2})
CB/CuPt-1	69	1.6×10^{-5}	515	562
CB/CuPt-2	53	1.6×10^{-6}	771	813
CB/Pt	82	3.9×10^{-6}	749	785
C/Pt10 commercial	89	1.5×10^{-5}	670	806

Considering the exchange current density values (i_0) presented in Table 5, it can be observed that the highest value is obtained for CB/CuPt-1, suggesting that this catalyst is thermodynamically the most active among the catalysts investigated, while the other bimetallic catalyst, CB/PtCu-2, seems to be less active. The same trend has been evidenced when the overpotential needed for a fixed hydrogen production rate at a current density of 1 mA cm^{-2} was considered, and the lowest overpotential is determined when CB/PtCu-1 was involved.

Fig. 7 displays the recorded cyclic voltammetry (CV) curves of CB/Pt, CB/PtCu-1 and CB-PtCu-2.
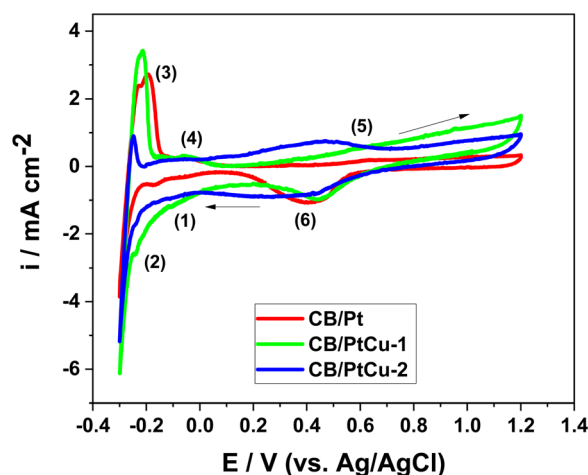

Fig. 7 Cyclic voltammograms of CB/Pt and CB/CuPt-1 and CB/CuPt-2 recorded in 0.1 M HClO$_4$ at a scan rate of 50 mV s^{-1}.

Table 6 ECSA values from CVs recorded at 50 mV s^{-1} in 0.1 M HClO$_4$

Electrocatalyst type	ECSA, m^2 g^{-1}
CB/Pt	13.89
CB/CuPt-1	27.32
CB/CuPt-2	12.65

Several peaks are observed in the investigated potential domain, in agreement with other literature data.[27] Peaks (1) and (2) are ascribed to the hydrogen electroadsorption process on the Pt surface while peaks (3) and (4) correspond to the electrodesorption process. Peak (5) is determined by the Pt oxidation and peak (6) is associated with the reduction of the formed Pt oxides.[27]

The ECSA values calculated using eqn (1) are presented in Table 6.

As shown in Table 6, CB/CuPt-1 demonstrates the highest ECSA value of 27.32 m^2 g^{-1}, larger than those of CB/Pt (13.89 m^2 g^{-1}) and CB/CuPt-2 (12.65 m^2 g^{-1}). The smaller ECSA in the case of CB/CuPt-2 could be caused by a stronger aggregation in the sample and therefore a smaller active area is accessible for the reactants.[18,39] In addition, a blockage of metal active sites by the presence of either un-alloyed Cu species or carbon overlayers on the surface is not excluded. The same behaviour has been reported for Pt$_4$Cu/C-based catalysts.[39]

The stability of the synthesized CB/Pt, CB/CuPt-1 and CB/CuPt-2 has been assessed *via* continuous potential cycling in acidic solution (Fig. 8). After 500 cycles, CB/CuPt-1 and CB/CuPt-2 showed a slight increase of the cathodic current as compared to CB/Pt, suggesting adequate stability of the composites.

In another series of experiments, the electrocatalytic activity of HER electrocatalysts was evaluated through direct measurement of the gas volumes involving Hofmann's cell. The cathodic efficiency of hydrogen quantity, produced during electrolysis using 0.5 M H$_2$SO$_4$ electrolyte, has then been determined for the synthesized composites under various applied current densities, as presented in Table 7.

The best HER efficiency could be observed in the case of CB/CuPt-1 and CB/CuPt-2. The increase of the applied current density facilitates a better cathodic efficiency, more pronounced when CB/CuPt-2 was involved, that attained 100%

Table 7 Cathodic efficiency of hydrogen evolution in 0.5 M H$_2$SO$_4$ electrolyte (η) for different values of the applied current

Electrode type	i/mA cm^{-2}	Time/s	Q/C	V_{H_2}/cm^3	η/%
CB/Pt	52.6	780	78	10.1	100
	263.1	540	270	23	67.2
CB/CuPt-1	50	780	78	8.5	85.9
	100	720	144	17.7	96.9
	250	420	210	26.5	99.5
CB/CuPt-2	50	900	90	10.5	92.1
	100	600	120	16	100
	250	480	240	39.8	100
C/Pt10 commercial	55.5	600	60	7.5	98.6
	172.7	600	186.6	23	97.2
	299.1	540	290.8	34.5	93.6

for 100–200 mA cm^{-2}. CB/Pt showed 100% HER efficiency at a relatively low current density of around 50 mA cm^{-2}, while at higher values (*i.e.* more than 250 mA cm^{-2}) the efficiency has been decreased down to about 67%.

4. Conclusions

In this work, we synthesized two hybrid copper–platinum composites and two mono-metallic control samples on the CB support with the use of the polyol-formaldehyde method. The two bi-metallic composites were prepared by two different experimental protocols: consecutive deposition of the two metals CB/CuPt-1 and co-deposition of CB/CuPt-2. With both methods, the use of copper facilitates deposition of platinum, leading to a higher platinum content in the products compared to the mono-metallic CB/Pt control sample, when the rest of the synthetic parameters were the same. SEM and HRTEM images show that, in monometallic CB/Cu, copper does not form any nanoparticles, being atomically dispersed on the CB surface. The other three samples have uniformly dispersed nanoparticles with a size of 2–4 nm, densely covering the CB support. XRD and XPS data suggest that copper facilitates more efficient reduction of platinum, and is incorporated into the nanoparticles.

Next, all the synthesized composites were tested in the HER. The two bi-metallic composites outperform not only the
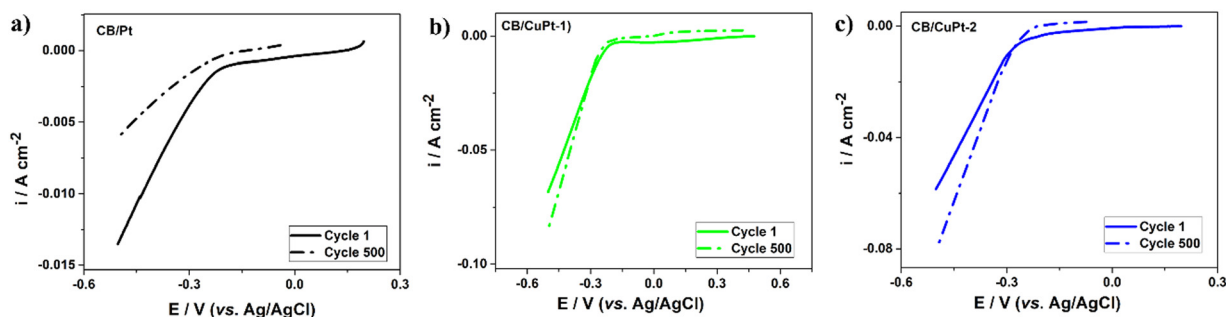

Fig. 8 The HER polarization curves of CB/Pt (a) and CB/CuPt (b) and (c) electrocatalysts before (solid lines) and after (dashed lines) 500 cycles in 0.5 M H$_2$SO$_4$ (scan rate = 100 mV s^{-1}).

mono-metallic CB/Pt sample, but also the commercial catalyst with a similar or even higher platinum content. Interestingly, the catalytic efficiency is not directly related to the platinum content in the tested materials. Thus, CB/CuPt-2 with a lower Pt content is more efficient in some parameters than CB/PtCu-1 with a higher Pt content. This observation suggests that incorporation of copper into the structure of the composite materials leads to the synergistic effects. Our results show the role of copper in the efficiency of the platinum catalysts for the HER and open the routes for increasing the efficiency of the hydrogen generation reaction on an industrial scale.

Data availability

The data supporting this article have been included as part of the ESI.†

Conflicts of interest

The authors declare no conflicts of interests.

Acknowledgements

References

1 N. Stetson and M. Wieliczko, Hydrogen technologies for energy storage: A perspective, *MRS Energy Sustainability*, 2021, **7**(1), E41.

2 R.-A. Felseghi, E. Carcadea, M. S. Raboaca, C. N. Trufin and C. Filote, Hydrogen Fuel Cell Technology for the Sustainable Future of Stationary Applications, *Energies*, 2019, **12**(23), 4593.

3 M. Yue, H. Lambert, E. Pahon, R. Roche, S. Jemei and D. Hissel, Hydrogen energy systems: A critical review of technologies, applications, trends and challenges, *Renewable Sustainable Energy Rev.*, 2021, **146**, 111180.

4 S. Anwar, F. Khan, Y. Zhang and A. Djire, Recent development in electrocatalysts for hydrogen production through water electrolysis, *Int. J. Hydrogen Energy*, 2021, **46**(63), 32284–32317.

5 P. K. Giesbrecht and M. S. Freund, Investigation of Hydrogen Oxidation and Evolution Reactions at Porous Pt/C Electrodes in Nafion-Based Membrane Electrode Assemblies Using Impedance Spectroscopy and Distribution of Relaxation Times Analysis, *J. Phys. Chem. C*, 2021, **126**(1), 132–150.

6 M. Liu, F. Hof, M. Moro, G. Valenti, F. Paolucci and A. Penicaud, Carbon supported noble metal nanoparticles as efficient catalysts for electrochemical water splitting, *Nanoscale*, 2020, **12**(39), 20165–20170.

7 J. N. Schwämmlein, B. M. Stühmeier, K. Wagenbauer, H. Dietz, V. Tileli, H. A. Gasteiger and H. A. El-Sayed, Origin of Superior HOR/HER Activity of Bimetallic Pt-Ru Catalysts in Alkaline Media Identified via Ru@Pt Core-Shell Nanoparticles, *J. Electrochem. Soc.*, 2018, **165**(5), H229–H239.

8 R.-Y. Shao, L.-W. Chen, Q.-Q. Yan, W.-J. Zeng, P. Yin and H.-W. Liang, Is Pt/C More Electrocatalytic than Ru/C for Hydrogen Evolution in Alkaline Electrolytes?, *ACS Appl. Energy Mater.*, 2021, **4**(5), 4284–4289.

9 R. Samanta, R. Mishra and S. Barman, Interface- and Surface-Engineered PdO–RuO(2) Hetero-Nanostructures with High Activity for Hydrogen Evolution/Oxidation Reactions, *ChemSusChem*, 2021, **14**(9), 2112–2125.

10 K. Eiler, S. Suriñach, J. Sort and E. Pellicer, Mesoporous Ni-rich Ni–Pt thin films: Electrodeposition, characterization and performance toward hydrogen evolution reaction in acidic media, *Appl. Catal., B*, 2020, **265**, 118597.

11 M. Sarno and E. Ponticorvo, Continuous flow HER and MOR evaluation of a new Pt/Pd/Co nano electrocatalyst, *Appl. Surf. Sci.*, 2018, **459**, 105–113.

12 Y. Jia, T. H. Huang, S. Lin, L. Guo, Y. M. Yu, J. H. Wang, K. W. Wang and S. Dai, Stable Pd-Cu Hydride Catalyst for Efficient Hydrogen Evolution, *Nano Lett.*, 2022, **22**(3), 1391–1397.

13 R. Huang, Z. Sun, S. Chen, S. Wu, Z. Shen, X. Wu and J. Zeng, Pt-Cu hierarchical quasi great dodecahedrons with abundant twinning defects for hydrogen evolution, *Chem. Commun.*, 2017, **53**(51), 6922–6925.

14 Y. Yang, Y.-F. Guo, C. Fu, R.-H. Zhang, W. Zhan, P. Wang, X. Zhang, Q. Wang and X.-W. Zhou, In-situ loading synthesis of graphene supported PtCu nanocube and its high activity and stability for methanol oxidation reaction, *J. Colloid Interface Sci.*, 2021, **595**, 107–117.

15 G.-X. Tian, Y. Yang, R.-H. Zhang, L.-Y. Yan, Z. Cheng, D.-H. Lin and X.-W. Zhou, Facile Hydrothermal Synthesis of Highly Efficient and Durable Ternary PtPdCu Electrocatalysts for the Methanol Oxidation Reaction, *Adv. Energy Sustainability Res.*, 2023, **4**(10), 2300058.

16 M. Asano, R. Kawamura, R. Sasakawa, N. Todoroki and T. Wadayama, Oxygen Reduction Reaction Activity for Strain-Controlled Pt-Based Model Alloy Catalysts: Surface Strains and Direct Electronic Effects Induced by Alloying Elements, *ACS Catal.*, 2016, **6**(8), 5285–5289.

17 X. Wang, Y. Zhu, A. Vasileff, Y. Jiao, S. Chen, L. Song, B. Zheng, Y. Zheng and S.-Z. Qiao, Strain Effect in Bimetallic Electrocatalysts in the Hydrogen Evolution Reaction, *ACS Energy Lett.*, 2018, **3**(5), 1198–1204.

18 X.-F. Zhang, A.-J. Wang, L. Zhang, J. Yuan, Z. Li and J.-J. Feng, Solvothermal Synthesis of Monodisperse PtCu Dodecahedral Nanoframes with Enhanced Catalytic Activity and Durability for Hydrogen Evolution Reaction, *ACS Appl. Energy Mater.*, 2018, **1**(9), 5054–5061.

19 D. Kaya, I. Demiroglu, I. B. Isik, H. H. Isik, S. K. Çetin, C. Sevik, A. Ekicibil and F. Karadag, Highly active bimetallic Pt–Cu nanoparticles for the electrocatalysis of hydrogen evolution reactions: Experimental and theoretical insight, *Int. J. Hydrogen Energy*, 2023, **48**(95), 37209–37223.

20 Y. Tuo, Q. Lu, C. Chen, T. Liu, Y. Pan, Y. Zhou and J. Zhang, The facile synthesis of core–shell PtCu nanoparticles with superior electrocatalytic activity and stability in the hydrogen evolution reaction, *RSC Adv.*, 2021, **11**(42), 26326–26335.

21 W. Li, Z.-Y. Hu, Z. Zhang, P. Wei, J. Zhang, Z. Pu, J. Zhu, D. He, S. Mu and G. Van Tendeloo, Nano-single crystal coalesced PtCu nanospheres as robust bifunctional catalyst for hydrogen evolution and oxygen reduction reactions, *J. Catal.*, 2019, **375**, 164–170.

22 Y. Du, K. Ni, Q. Zhai, Y. Yun, Y. Xu, H. Sheng, Y. Zhu and M. Zhu, Facile air oxidative induced dealloying of hierarchical branched PtCu nanodendrites with enhanced activity for hydrogen evolution, *Appl. Catal., A*, 2018, **557**, 72–78.

23 H. Zhang, X. Guo, W. Liu, D. Wu, D. Cao and D. Cheng, Regulating surface composition of platinum-copper nanotubes for enhanced hydrogen evolution reaction in all pH values, *J. Colloid Interface Sci.*, 2023, **629**, 53–62.

24 L. Liu, Y. Wang, Y. Zhao, Y. Wang, Z. Zhang, T. Wu, W. Qin, S. Liu, B. Jia, H. Wu, D. Zhang, X. Qu, M. Chhowalla and M. Qin, Ultrahigh Pt-Mass-Activity Hydrogen Evolution Catalyst Electrodeposited from Bulk Pt, *Adv. Funct. Mater.*, 2022, **32**(20), 2112207.

25 C. Zhang, Q. Liu, P. Wang, J. Zhu, D. Chen, Y. Yang, Y. Zhao, Z. Pu and S. Mu, Molybdenum Carbide-PtCu Nanoalloy Heterostructures on MOF-Derived Carbon toward Efficient Hydrogen Evolution, *Small*, 2021, **17**(51), 2104241.

26 M. Zhou, Y. Zhao, X. Zhao, P.-F. Yin, C.-K. Dong, H. Liu, X.-W. Du and J. Yang, Dislocation-Activated Low Platinum-Loaded PtCu Nanoparticles Welded onto the Substrate for Practical Acidic Hydrogen Generation, *ACS Appl. Energy Mater.*, 2024, **7**(9), 3848–3857.

27 J. Zhang and J. Zhang, in Catalyst Layer/MEA Performance Evaluation, ed J. Zhang, *PEM Fuel Cell Electrocatalysts and Catalyst Layers: Fundamentals and Applications*, Springer London, London, 2008, pp. 965–1002.

28 V. E. Guterman, S. V. Belenov, A. Y. Pakharev, M. Min, N. Y. Tabachkova, E. B. Mikheykina, L. L. Vysochina and T. A. Lastovina, Pt-M/C (M = Cu, Ag) electrocatalysts with an inhomogeneous distribution of metals in the nanoparticles, *Int. J. Hydrogen Energy*, 2016, **41**(3), 1609–1626.

29 B. Yazici, G. Tatli, H. Galip and M. Erbil, Investigation of suitable cathodes for the production of hydrogen gas by electrolysis, *Int. J. Hydrogen Energy*, 1995, **20**(12), 957–965.

30 T. Ungár, J. Gubicza, G. Ribárik, C. Pantea and T. W. Zerda, Microstructure of carbon blacks determined by X-ray diffraction profile analysis, *Carbon*, 2002, **40**(6), 929–937.

31 B. D. Cullity and S. R. Stock, *Elements of X-Ray Diffraction*, Prentice Hall, Upper Saddle River (NJ), 3rd edn, 2001.

32 A. R. Denton and N. W. Ashcroft, Vegard's Law, *Phys. Rev. A*, 1991, **43**, 3161.

33 S. Lan, C. Groschner, J. Runco, A. Wise, M. Diaz-Michelena, D. Laughlin and M. E. McHenry, Phase Identification and Temperature-Dependent Magnetization of Ti-Rich Titanomagnetite (0.5 ≤ x ≤ 1) in Different Atmospheres, *IEEE Trans. Magn.*, 2013, **49**(7), 4314–4318.

34 J. O. Bockris, A. K. N. Reddy and M. E. Gamboa-Aldeco, *Modern Electrochemistry*, Plenum Press, 1998.

35 S. Anantharaj, S. Noda, M. Driess and P. W. Menezes, The Pitfalls of Using Potentiodynamic Polarization Curves for Tafel Analysis in Electrocatalytic Water Splitting, *ACS Energy Lett.*, 2021, **6**(4), 1607–1611.

36 E. Navarro-Flores, Z. Chong and S. Omanovic, Characterization of Ni, NiMo, NiW and NiFe electroactive coatings as electrocatalysts for hydrogen evolution in an acidic medium, *J. Mol. Catal. A*, 2005, **226**(2), 179–197.

37 C. Wan, Y. Ling, S. Wang, H. Pu, Y. Huang and X. Duan, Unraveling and Resolving the Inconsistencies in Tafel Analysis for Hydrogen Evolution Reactions, *ACS Central Sci.*, 2024, **10**(3), 658–665.

38 Y. Zheng, Y. Jiao, M. Jaroniec and S. Z. Qiao, Advancing the Electrochemistry of the Hydrogen-Evolution Reaction through Combining Experiment and Theory, *Angew. Chem., Int. Ed.*, 2015, **54**(1), 52–65.

39 Q. Liu, J. Tripp, C. Mitchell, P. Rzepka, I. I. Sadykov, A. Beck, F. Krumeich, S. Nundy, L. Artiglia, M. Ranocchiari and J. A. van Bokhoven, Influence of alloying and surface overcoating engineering on the electrochemical properties of carbon-supported PtCu nanocrystals, *J. Alloys Compd.*, 2023, **968**, 172128.